Nuclear Instruments and Methods in Physics Research A 343 (1994) 401–414
North-Holland

NUCLEAR INSTRUMENTS & METHODS IN PHYSICS RESEARCH
Section A

A residual-gas ionization beam profile monitor for the Heidelberg Test Storage Ring TSR

B. Hochadel, F. Albrecht, M. Grieser, D. Habs, D. Schwalm, E. Szmola [1], A. Wolf *

Max-Planck-Institut für Kernphysik and Physikalisches Institut der Universität Heidelberg, D-69029 Heidelberg, Germany

(Received 22 November 1993)

A monitoring device for the transverse density distribution of stored heavy-ion beams, based on the detection of ionization products of the beam particles in the residual gas, has been developed for the heavy-ion Test Storage Ring (TSR) in Heidelberg. With two monitor units installed in the ring, non-destructive, sensitive measurements of the horizontal and vertical profiles of cooled stored ion beams can be performed with a spatial resolution of about $\pm(0.2–0.3)$ mm. The beam profile monitors are used to determine the transverse beam temperature, to study transverse cooling and heating mechanisms, to observe the ion beam behaviour during experiments, and to determine storage-ring parameters such as the dispersion function. The principle, technical realization and operation of these devices are described. First experimental results concerning transverse electron cooling of heavy-ion beams are discussed, in particular the measurement of cooling rates and the optimization of the alignment between the stored ion beam and the cooling electron beam.

1. Introduction

The Heidelberg Test Storage Ring (TSR) [1] can store a large variety of fast heavy-ion beams with a magnetic rigidity up to 1.7 T m. The ring with a circumference of 55.4 m, shown in Fig. 1, is used for highly charged ions with a charge-to-mass ratio $q/A \approx 1/2$ (specific energy up to 30 MeV/u) as well as for single-charged heavy ions with typically $q/A \lesssim 1/7$ (specific energy $\lesssim 2$ MeV/u). One of the main topics of the experimental program at the TSR [2] is the development of beam cooling techniques, in particular electron cooling [3,4] and laser cooling [5–7], and the study of the properties of cold, dense ion beams. Moreover, the high phase-space density of stored and cooled heavy-ion beams is opening up many new possibilities for experiments in the fields of atomic and nuclear physics [2].

Non-destructive diagnostic methods for stored ion beams [8] are of great importance both for systematic studies of beam cooling and for the set-up of storage-ring experiments with cooled heavy ions. A number of ion-beam properties can be monitored conveniently by observing the fluctuations of electronic signals induced by the ion beam in suitable pick-up electrodes or coils. The Schottky-noise spectrum of the ion beam [9] observed at a "longitudinal" pick-up, responding to fluctuations of the total beam intensity, is commonly used to determine the longitudinal momentum spread of a coasting ion ensemble. The signal generated by a suffiently intense, bunched beam in a "transverse"

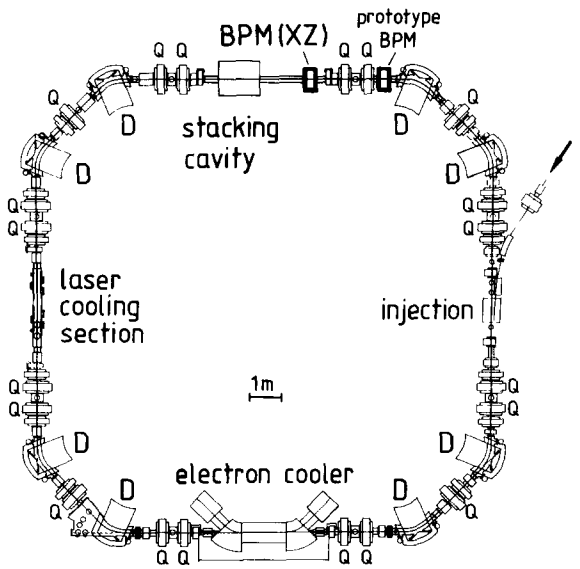

Fig. 1. Schematic drawing of the Heidelberg Test Storage Ring TSR with the prototype BPM, the two-dimensional monitor BPM(XZ), and D: dipole magnets, Q: quadrupole magnets.

* Corresponding author.
[1] Now at GEL-E-BRC (Bródy Research Center), H-1340 Budapest, Hungary.

SSDI 0168-9002(93)E1294-8

pick-up, responding to the centroid of the transverse density profile, can be processed to yield the ion beam position [8]. In some cases, the Schottky-noise spectrum of a coasting beam induced in a transverse pick-up can serve to measure even the root-mean-square (r.m.s.) beam size, reflected by the amplitude of the betatron sidebands [9]. However, for electron-cooled ion beams of typical diameters of ≈ 1 mm and correspondingly small betatron oscillation amplitudes, this method fails as the sidebands become too weak to be detectable; hence, there seems to be no access to the transverse properties of such beams using electronic pick-ups.

A powerful method for non-destructive beam diagnostics, in particular for the transverse density profile of stored ion beams, is the spatially resolved detection of the ionization products produced by the circulating ions in the residual gas. In high-energy proton synchrotrons, generally operating at a relatively high residual-gas pressure of $\gtrsim 10^{-9}$ mbar, ionization beam-profile monitors are widely used [10–12]. At better vacua, such as in the CERN intersecting storage rings (ISR) [13], a vapour target was used to generate a local increase of the background gas density. Similar profile monitors were also used in early electron cooling experiments [14,15].

Heavy-ion storage rings generally operate at a very low residual-gas pressure of the order of 10^{-11} mbar. In order to obtain nevertheless sufficient sensitivity and a large dynamic range for the detection of the ionization products, the type of beam profile monitor described here employs single-particle counting. In addition, as will be shown below, the sensitivity of ionization monitors in heavy-ion storage rings is improved in comparison to high-energy proton rings by the increase of the ionization yield of the circulating ions due to their higher charge and their relatively low velocity.

In section 2 we will give a short discussion of the principle of operation, the sensitivity, and the spatial resolution of ionization profile monitors for heavy-ion beams. We will then describe the design and the technical realization of the monitors developed for the TSR (section 3). The analysis of ion-beam properties based on beam profile measurements and first experimental results, concerning in particular transverse electron cooling of heavy ions, will be discussed in section 4.

2. Principle of ionization beam profile monitors for heavy ions

The principle of a residual-gas ionization beam profile monitor is illustrated in Fig. 2. The circulating beam crosses the free volume between two parallel metal plates. High voltage applied to the plates results in a homogeneous electric field $\mathscr{E}$ perpendicular to the beam direction. Residual-gas ions produced in collisions of residual-gas molecules with the stored ions are accelerated by the electric field into a position-sensitive detector mounted on one plate. That leads to a projection of the beam profile into the detector, because the number of liberated residual-gas ions in a given volume is proportional to the density of the incident ion beam.

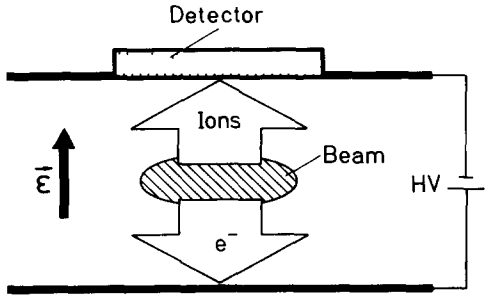

Fig. 2. Principle of an ionization beam profile monitor. Residual-gas ions produced by the stored ion beam are accelerated into a position-sensitive detector.

To judge whether this method is suitable for typical storage-ring conditions, the rate N_D of liberated ions hitting the detector surface and the spatial resolution limit Δx must be estimated. The ion rate N_D can be calculated from the residual-gas pressure, the residual-gas composition, the ionization cross-section, the properties of the ion beam and the geometry of the detector. For ultra-high vacuum conditions the residual gas predominantly consists of H_2, and in the case of the TSR the fraction of H_2 is about 90% at a pressure of $\approx 5 \times 10^{-11}$ mbar. Therefore, a restriction to hydrogen molecules seems to be appropriate for a first estimate. The interesting ionization processes are

$$I^{q+} + H_2 \rightarrow \begin{cases} I^{q+} + H_2^+ + e^-; \\ I^{q+} + H + H^+ + e^-; \end{cases} \quad (1)$$

where, in the velocity range relevant here, the non-dissociative process dominates by at least a factor of five [16]; moreover, double ionization and transfer ionization reactions can be neglected in the energy range of interest here. The impact of protons on atomic hydrogen,

$$H^+ + H \rightarrow H^+ + H^+ + e^-, \quad (2)$$

is a prototype reaction for process (1). The ionization cross-section $\sigma^{H^+ + H}$ is well known [17], and in the ion energy range from ≈ 0.2 to ≈ 100 MeV/u the cross section $\sigma^{I^{q+} + H_2}$ for the ionization of hydrogen molecules can be derived in good approximation from $\sigma^{H^+ + H}$ given by

$$\sigma^{H^+ + H}(E) \approx 2 \times 10^{-17}\ \mathrm{cm}^2 (E/\mathrm{MeV})^{-1}, \quad (3)$$

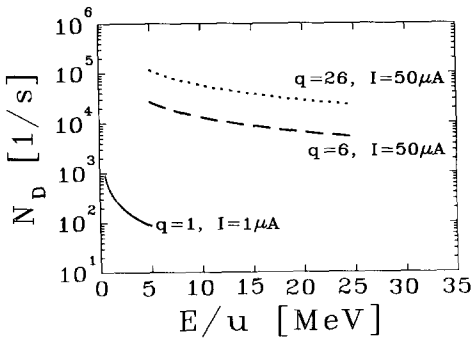

Fig. 3. Rate N_D of ions produced by the circulating beam on the detector surface of a profile monitor of active length of $l = 15$ mm calculated as a function of the specific energy E/A for the beam-current and energy range typical for highly charged as well as for single-charged ions, assuming a H_2 residual-gas pressure of 5×10^{-11} mbar.

using the scaling law [17]

$$\sigma^{I^{q+}+H}(E) = q^2 \sigma^{H^+ + H}(E/A), \tag{4}$$

and assuming

$$\sigma^{I^{q+}+H_2}(E) \approx 2\sigma^{I^{q+}+H}(E). \tag{5}$$

Here, E denotes the ion energy and A the ion mass number. The rate of ions on the detector surface, N_D, is then given by

$$N_D = (I/qe) n l \sigma^{I^{q+}+H_2}(E), \quad n = p/k_B T, \tag{6}$$

where I is the beam current, qe the ion charge, l the length of the detector in beam direction and n the density of the residual gas, determined by the pressure p, the temperature T and the Boltzmann constant k_B.

For completeness it should be mentioned that the cross section for proton impact increases for $E > 1$ GeV because of relativistic effects and cannot be described any longer by the scaling law (3). An estimate of the count rate can then be obtained for example from the Sternheimer range–energy relationship [18] and assuming that 95 eV are required on average to produce an ion pair [10].

Estimates of the ion rate at the detector surface using Eq. (6) are presented in Fig. 3 for two typical situations at the TSR, namely for highly charged ions with a charge-to-mass ratio $q/A \approx 1/2$ and specific energies $\lesssim 30$ MeV/u, and for single-charged ions with typically $q/A \lesssim 1/7$ and specific energies $\lesssim 2$ MeV/u. The ion rate as a function of the energy per nucleon for highly charged ions with $q = 26$ (dotted line) and $q = 6$ (dashed line) was calculated assuming a typical current of about 50 μA reached by accumulation techniques, a gas pressure of 5×10^{-11} mbar, and a detector length l of 15 mm. Also plotted (full line) is the ion rate for single-charged ions at a lower beam current of 1 μA, which is typical for these beams since their lifetime is too short to allow for an extensive ion accumulation. In comparison to earlier applications of ionization beam profile monitors [10–12], where microchannel plate (MCP) detectors with fluorescent screens and optical readout could be used, the ion rates at the TSR are relatively low. Hence, we decided to operate the MCP in a *single-ion counting* mode in order to increase the sensitivity. With the count rate of 10^4–10^5 s^{-1} reached for beams of highly charged ions at ≈ 50 μA, beam profiles can then be recorded in short measuring times of 1 s or less. In fact, since this rate is close to the maximum count rate permitted by the channel plate and the readout electronics, it may even be necessary to reduce the beam intensity during the profile measurements. For single-charged-ion currents of 1 μA, on the other hand, the count rate of ≈ 300 s^{-1} is still sufficient to obtain beam profiles in measuring times of the order of 10 s; in fact, reasonable profile measurements are still possible at ion currents much below 1 μA.

The spatial resolution is limited in principle by the transverse momentum transfer to the residual-gas ions during the ionization process and by the thermal motion of the residual gas. Velocity components transverse to the beam direction and parallel to the metal plates result in a lateral displacement Δx at the detector referring to the position where the ionization process took place, as shown in Fig. 4. This displacement is given by

$$\Delta x = \sqrt{2M\Delta z/e\mathscr{E}}\, v_\perp, \tag{7}$$

where $v_\perp$ and M denote the transverse velocity component and the mass of a residual-gas ion, respectively, Δz is the initial distance between the residual gas ion and the detector, and $\mathscr{E}$ is the electric field strength in the detection volume.

The energy range of the recoiling residual-gas ion can be estimated from the impact-parameter range of

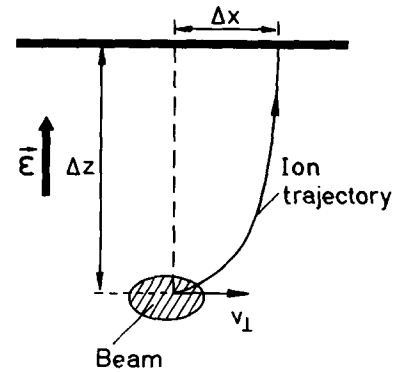

Fig. 4. Limitation of the spatial resolution by a velocity component $v_\perp$ of a residual-gas ion transverse to the beam direction

the ionization process, considering the Coulomb interaction between the incident ion and the recoil ion at the corresponding distance. The effective minimum impact parameter in the velocity region of interest is approximately given by $2qa_0\alpha c/v_0$ [19], where a_0 is the Bohr radius, α the fine-structure constant, c the velocity of light, and v_0 the beam velocity. The value of the maximum recoil energy obtained in this approximation is independent of the velocity and the charge of the stored ions and amounts to ≈ 4 meV for H_2 recoil ions. For the design values $\mathscr{E} = 2$ kV/cm and $\Delta z = 2.5$ cm, the r.m.s. spatial spread caused by this energy transfer can be estimated to be $\Delta x_{\mathrm{rec}} \approx 30$ μm. The contribution to the r.m.s. spread due to the thermal motion follows from Eq. (7) to be about $\Delta x_{\mathrm{th}} \approx 70$ μm. Both contributions are small compared to the intrinsic resolution limit of the detector and the readout electronics, which was determined before the installation into the TSR to be $\Delta x_{\mathrm{el}} = 250(50)$ μm. Hence, the spatial resolution can be expected to be limited by the total r.m.s. spread of

$$\Delta x_{\mathrm{tot}} = \sqrt{(\Delta x_{\mathrm{rec}})^2 + (\Delta x_{\mathrm{th}})^2 + (\Delta x_{\mathrm{el}})^2} \approx 260(50)\ \mu\mathrm{m}. \quad (8)$$

It should be mentioned that in principle it is also possible to detect the liberated electrons. However, the initial transverse velocity components of the electrons are much higher than for the residual gas ions, and from differential cross sections [20] a spatial resolution of ≈ 1–1.5 mm can be estimated. Therefore, profile measurements by detecting electrons are inappropriate at the TSR, where the full width at half-maximum (FWHM) beam diameters for electron-cooled ion beams are of the order of 1 mm. Measurements of the resolution for ion detection, which confirm the upper estimates, are presented in section 4.1.1.

3. Technical realization

3.1. Imaging component

Two beam profile monitors, a prototype with one-dimensional spatial resolution in the horizontal plane and the final instrument with both horizontal and vertical spatial resolution, were installed in the TSR at the positions marked in Fig. 1; they are denoted "prototype BPM" and "BPM(XZ)" in the following. A view of the imaging component of the prototype BPM is shown in Fig. 5. It consists of two parallel metal plates in the horizontal plane and additional equally-spaced field-shaping electrodes. The stored ion beam crosses the free volume between the plates parallel to the field-shaping electrodes. The dimensions of the detector plate and the end plate are 100×160 mm; they have a distance of 50 mm. A round opening in the detector plate gives access to the full active area of the multichannel plate (MCP) with a diameter of 40 mm. A resistive anode behind the MCP yields a one-dimensional spatial resolution transverse to the beam direction. The surface of the MCP has electrical contact to the detector plate. In front of the detector four calibration wires with a diameter of 1 mm are mounted parallel to the beam direction.

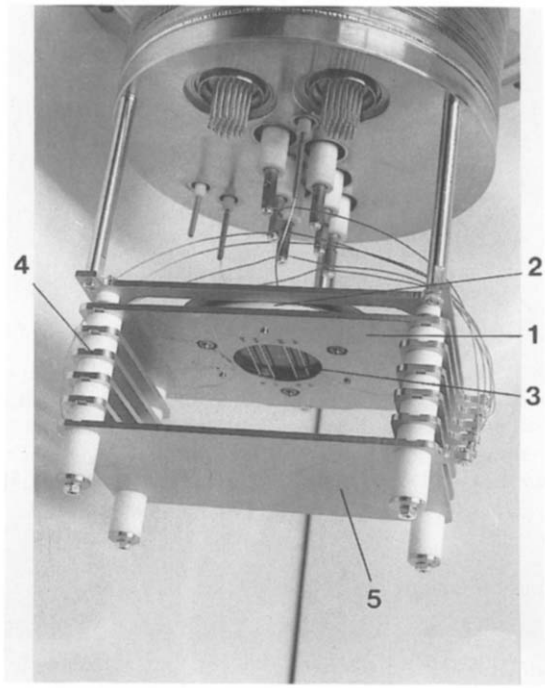

Fig. 5. Imaging component of the prototype BPM: (1) detector plate, (2) microchannel-plate detector, (3) calibration wire, (4) field-shaping electrode, (5) end plate.

The material as well as the machining and assembling procedures were carefully chosen to fulfill the ultra-high vacuum requirements of the TSR, aiming at residual-gas pressures below 10^{-11} mbar. The monitor is bakeable in-situ at 300°C and its vacuum vessel is equipped with sublimation and ion getter pumps. Being mounted on a flange connected to a bellow and a pneumatic drive, the imaging component can be moved in and out of the beam tube in vertical direction, because for certain operating modes of the storage ring the entire aperture of the vacuum chamber (20 cm diameter) may be required. The imaging component fits into a vacuum chamber of 35 cm length, corresponding to the size of a standard diagnostic chamber at the TSR.

3.2. High-voltage system

The high-voltage system of the imaging component is shown in Fig. 6. A positive voltage of typically 10 kV is applied to the end electrode by power supply PS1 [21]. In order to keep the resulting electric field homogenous over the active volume, the potential on the field-shaping electrodes is gradually reduced towards the detector plate by means of a voltage divider mounted across the vacuum feedthroughs on the atmospheric side.

The bias voltage of the detector is generated by a separate power supply PS3 [23] in order to avoid additional noise which might be caused by PS1 and to have the possibility of an independent control of the detector bias. Correspondingly, PS1 has a floating ground-potential defined by PS2 [24], which must be set at the same voltage as PS3 to maintain a constant gradient of the electric field. Finally, an additional power supply PS4 [23] is needed to pull the electrons from the exit of the MCP to the detector anode which is operated close to ground (see section 3.3).

Without a suitable correction, the small deflection of the stored ions in the electric field of the monitors at each passage would lead to a complete loss of the beam intensity. However, the effect of the deflection can easily be compensated for using the correction dipoles of the TSR.

3.3. Detector

Based on the estimates of the ion rate in section 2, a chevron MCP assembly [25] consisting of two microchannel plates in series was chosen to detect the residual gas ions (Fig. 7). It provides an amplification of $\approx 10^7$, necessary for the electronic detection of single residual-gas ions impinging on the active surface, it operates over a wide range of count rates, and allows for good spatial resolutions. The detection efficiency for hydrogen ions of 5 keV is estimated to be 60–85% [26]. The bias voltage of the channelplates is determined by the difference of the voltages defined by PS3 and PS4 (see Fig. 6) and is adjusted to 1000 V per plate. The electron cloud resulting from an incident ion is accelerated onto the resistive anode (RA) mounted a few mm behind the MCP. The RA consists of a resistive sheet on a ceramic substrate. Electrical contact is made to two electrodes at the opposite ends of the sheet (total resistance $\approx 200\ \mathrm{k}\Omega$) and to a rear metal plate providing a capacitive coupling of the resistive layer to ground. Tests suggested a value of 300 V for the acceleration potential between MCP and RA (set by PS4) to ensure an optimum spatial resolution. Among the various possibilities available for a position sensitive readout of channelplates, a resistive anode was chosen mainly for practical reasons. The RA enables one to use a straightforward method for the readout, which will be described in the next section. Furthermore the number of elements in the vacuum chamber is minimized. The RA requires only two signal lines and therefore only two ultra-high vacuum feedthroughs, while the necessary shielding of the sig-

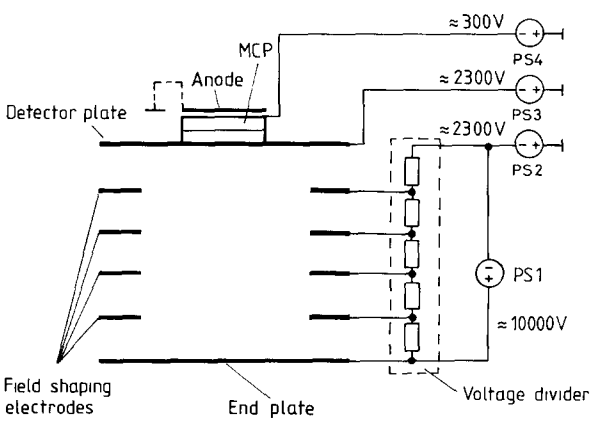

Fig. 6. High-voltage system of the imaging component with typical operating voltages (PS: power supply, MCP: multichannel plate).

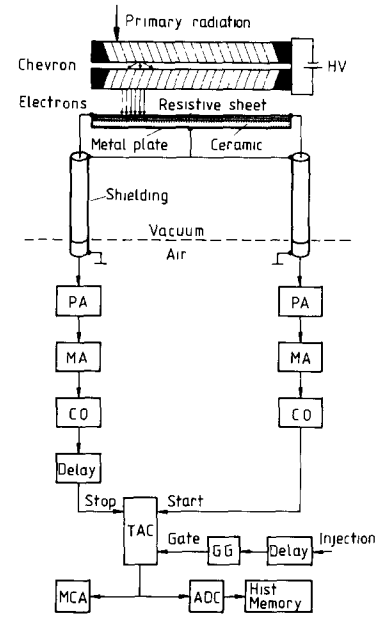

Fig. 7. Chevron microchannel-plate assembly and block diagram of the readout electronics for the pulse rise-time method (see also the text; PA: charge-sensitive pre-amplifier, MA: spectroscopy main amplifier, CO: single-channel analyzer in cross-over mode, TAC: time-to-amplitude converter, GG: gate generator, ADC: analog–digital converter, MCA: multichannel analyzer).

nal lines in the vacuum chamber can be realized without too much technical effort.

3.4. Readout

Position signals from the resistive anode can be derived by two readout techniques, namely the charge-division and the rise-time method. The charge-division method in one dimension makes use of two charge-sensitive preamplifiers to integrate the charges at each end of the resistive strip; after pulse shaping, an analog circuit computes $x/L = q_1/(q_1 + q_2)$, where x is the event location and q_1 and q_2 are the charge amplitudes at both ends of the resistive strip of length L. However, for the beam profile monitors at the TSR the rise-time method is used, which can be realized more easily using standard NIM electronic modules. This method is based on measuring the difference of the rise-times of the pulses occurring at each end of the resistive sheet, which are proportional to x and $L - x$, respectively. Fig. 7 shows a block diagram of the readout electronics used to measure the difference of pulse rise-times, which was mainly adapted from ref. [26]. Charge pulses at each end of the resistive anode are integrated in charge-sensitive preamplifiers (PA), whose output pulses are shaped by spectroscopy main amplifiers (MA) with bipolar output. The zero-crossing times of the amplifier output pulses represent the rise times of the input signals. The zero crossings are detected by single-channel analyzers in cross-over mode (CO), which generate fast logic pulses used to start and stop a time-to-amplitude converter (TAC). The pulse-height spectrum of the TAC output pulses represents the spatial distribution of the ions detected by the MCP and can for example be displayed on a multichannel pulse-height analyzer (MCA). To measure at well-defined times after beam injection, the TAC is gated by a logic pulse derived from the injection time using a gate generator (GG). In ref. [27], where a RA is considered to be a diffusive RC line, it is shown that optimum performance (linearity and spatial resolution) using the rise-time encoding technique is expected when $T_0 = RC/\pi^2$, where T_0 is the shaping time constant of the bipolar amplifiers, R denotes the total resistance of the resistive sheet between the two readout electrodes, and C is the capacitance defined by the rear metal plate. The RA used here is designed for 1 $\mu s < T_0 < 2$ μs, which is a range easily accessive with standard NIM modules. This choice however limits the maximum count-rate capability of each imaging unit to about 50 kHz.

3.5. Description of the two-dimensional monitor BPM(XZ)

The layout of the two-dimensional monitor BPM(XZ), equipped to measure both the horizontal and the vertical density profile of the ion beam, is shown in Fig. 8. It consists of two independent imaging components with the detector planes rotated by an angle of 90° with respect to each other.

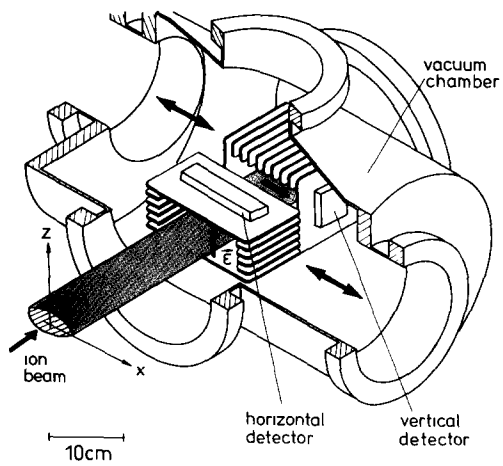

Fig. 8. Perspective view of BPM(XZ) for measuring horizontal and vertical beam profiles. Each imaging unit can be seperabely moved out of the beam path as indicated by the double-head arrows

A view of the horizontal component of BPM(XZ) is shown in Fig. 9a. A rectangular MCP with a resistive anode is used [25]. The active area is 15×100 mm corresponding to the slit in the detector plate. The relatively large width of 100 mm was found to be necessary from the experience made with the prototype BPM, where the active area of 40 mm for the MCP often was too small to detect the complete horizontal profile of uncooled beams injected with multiturn injection, which is the standard injection mode at the TSR [28]. The dimensions of the detector plate and the end plate are 85×160 mm, the distance between them is 50 mm.

The vertical component is shown in Fig. 9b. The same MCP type as in the case of the prototype BPM is used [25]. The full active area of a diameter of 40 mm is open to the residual-gas ions. This size also covers the maximum extension of uncooled beams in the vertical degree of freedom, which is much less affected by the multiturn injection than the horizontal one. The dimensions of the detector plate and the end plate are 100×100 mm; the distance between them is 110 mm. Two calibration wires with a diameter of 0.6 mm are mounted in front of the active area of the MCP.

The arrangement of the two imaging components was chosen such that the electric field distributions in the active volumes are affected by each other only weakly. To study this mutual influence, three-dimensional electric-field calculations have been performed with a suitable computer code [22]. These calculations

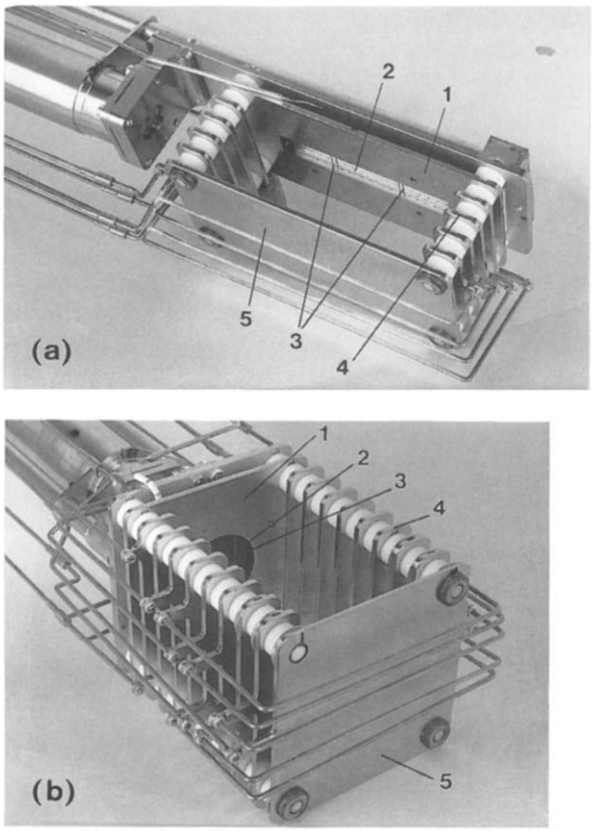

Fig. 9. Horizontal (a) and vertical (b) imaging components of BPM(XZ): (1) detector plate, (2) microchannel-plate detector, (3) calibration wires, (4) field-shaping electrodes, (5) end plate

have shown that despite the relatively close mounting, the field homogeneity obtained in both detection volumes is sufficient to ensure a proper functioning of the units. Each imaging component can seperately be moved in and out of the beam tube in horizontal direction. The two components fit into a vacuum chamber of 35 cm length. The high-voltage system and the readout of the imaging components correspond to those described in sections 3.2–3.4.

4. Experimental results

In this section we will first discuss experimental results concerning the performance of the profile monitors (section 4.1) and then turn to their application in the study of electron-cooled ion beams (section 4.2).

4.1. Performance of the beam profile monitor

For a proper interpretation of measured beam profiles it is important to have exact knowledge of the spatial resolution, the position linearity and the sensitivity. The results obtained for these quantities are described in the following.

4.1.1. Spatial resolution

An upper limit of the spatial resolution which can be obtained in beam profile measurements is given by the smallest detected profiles. Since the equilibrium size of electron-cooled ion beams increases with their intensity, only profiles measured at a very low beam current are possibly dominated by the detector resolution. A few examples are shown in Fig. 10. Up to now the lowest measured r.m.s. radii are 0.30(5) mm for the prototype BPM and 0.21(4) mm and 0.29(6) mm for the

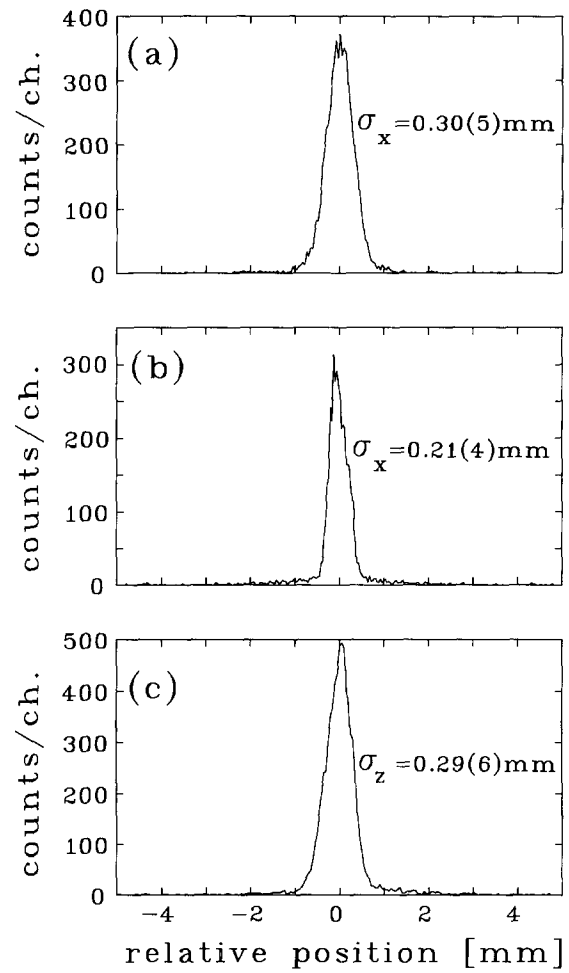

Fig. 10. Beam profiles representing the lowest r.m.s. radii σ_x, σ_z measured at the TSR: (a) horizontal profile (prototype BPM) of a 0.81 MeV/u $^9Be^+$ ion beam, $I \approx 1$ μA, measuring time 10 s, channel width 0.047 mm; (b) horizontal and (c) vertical profile [BPM(XZ)] of a 1.9 MeV/u $^7Li^+$ beam, $I \ll 1$ μA, measuring time 50 s, channel widths 0.036 mm (b) and 0.05 mm (c).

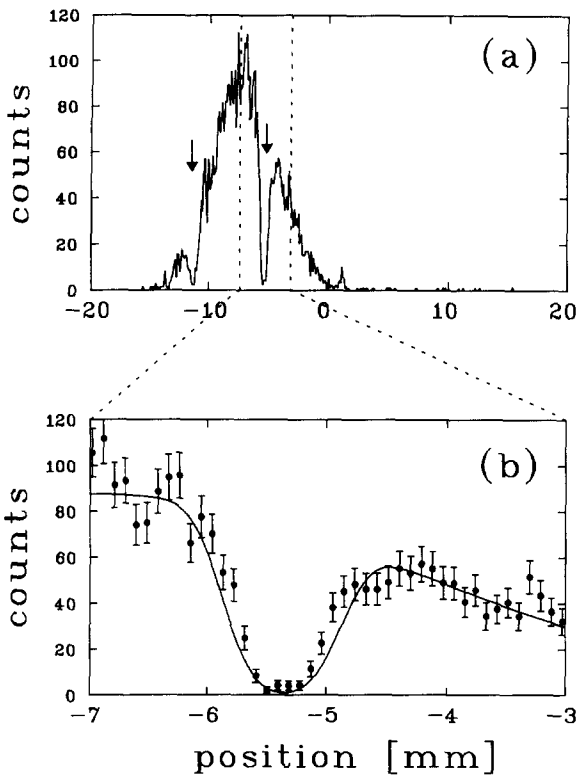

Fig. 11. (a) Beam profile with dips (indicated by arrows) caused by the calibration wires of the prototype BPM. (b) Data points close to a calibration dip together with a fitted curve discussed in the text. From this fit the intrinsic resolution limit of the detector is determined.

horizontal and vertical profile of BPM(XZ), respectively.

The intrinsic resolution limit Δx_{el} of the detectors and the readout electronics was determined in previous detector tests and can also be derived from the shape of the dips due to the calibration wires, which appear in the profiles of ion beams with large beam diameters. As an example a horizontal profile taken with the prototype BPM is shown in Fig. 11a. The data points were fitted (see Fig. 11b) by folding the theoretically expected shape at infinite resolution with a Gaussian curve representing the detector resolution function and adjusting its standard deviation. Using this method Δx_{el} was determined to 0.25(5) mm for the detector of the prototype BPM and also for both detectors of BPM(XZ). The upper limits for the total r.m.s. resolution determined from the profiles of cold, low-intensity ion beams are in good agreement with the estimate of Eq. (8) and show the expected dominance of the intrinsic detector resolution Δx_{el}.

4.1.2. Non-linearity

The linearity could be checked using the measured positions of the dips due to the calibration wires (see Fig. 11a) and was determined more precisely in preliminary tests of the detectors and the readout electronics by covering the MCPs with a slit mask and irradiating them by α particles. For each detector the measured positions as a function of the expected positions were found to deviate from a fitted straight line only within the experimental error (≈ 0.05 mm) over the whole active areas of the MCPs. Thus, the readout of the event positions on the RA is shown to be linear within the experimental accuracy.

4.1.3. Sensitivity

The beam profile monitors are the most sensitive instruments to measure low-intensity beams in the TSR. Even single-charged ions with a small ionization cross-section (see section 2) and beam currents < 1 μA can be detected with reasonable statistics and time resolution. For example, the rate for a $^9Be^+$ beam of 0.81 MeV/u was measured at the prototype BPM to be $\approx 800\ s^{-1}$ for 0.5 μA corresponding to 1.5×10^6 stored particles, while the background rate was found to be negligibly small. The estimates of N_D presented in section 2 gave the right order of magnitude for all beams studied. Because of their high sensitivity, a measurement of the total ion count-rate by either one of the monitors, after a suitable calibration, can yield the current and lifetime of coasting ion beams in an intensity range where other methods, such as dc beam-current transformers [8], fail.

4.2. First applications

The main application of the beam profile monitors is the measurement of the emittance and the average transverse temperature of the ion beam. In the following we will first discuss the relation between the width of the transverse density profile as measured by the monitor and the ion velocity spread in the rest frame of the stored beam. We will then consider the transverse electron cooling of heavy ions and present first measurements of the transverse cooling rate and of the general properties of the transverse cooling force using the beam profile monitor. Moreover, a procedure of aligning the ion and the electron beam in order to optimize the electron cooling process will be discussed. Both the cooling-rate and the alignment measurements allow us to draw conclusions on the effective electron temperature of the cooling electron beam.

4.2.1. Ion beam emittance and temperature

For small deviations from the equilibrium orbit, the transverse coordinate x of an ion as a function of the

distance s travelled in the beam direction can be written as [29]

$$x(s) = \sqrt{\epsilon_x \beta_x(s)/\pi}\,\cos[\psi_x(s) + \phi_x] + D_x(s)(p - p_0)/p_0, \quad (9)$$

where ϵ_x is the invariant action of the oscillatory motion in the x direction, ϕ_x the phase constant of this motion, and $\beta_x(s)$ and $D_x(s)$ are the lattice functions of the storage ring, which are periodic over the circumference C of the ring and follow from the arrangement of the dipole and quadrupole magnets. The dispersion function $D_x(s)$ describes the position of the equilibrium orbit of an ion with the momentum deviation $p - p_0$ relative to the reference orbit of an ion having the nominal momentum p_0. Eq. (9) applies both to the horizontal and the vertical ion motion, although the dispersion in the vertical direction can usually be neglected. The first term in Eq. (9) represents the betatron oscillations which, in the approximation considered here, proceed independently of each other in the two transverse directions. The phase advance of the betatron oscillation is given by $\mathrm{d}\psi_x(s)/\mathrm{d}s = 1/\beta_x(s)$.

For an ensemble of circulating ions the lattice function $\beta_x(s)$ describes the variation of the beam envelope around the ring due to the magnetic focusing. In particular, for a Gaussian transverse density distribution and a Gaussian longitudinal momentum distribution with a r.m.s. width of σ_p, the standard deviation $\sigma_x(s)$ of the beam profile is given by

$$\sigma_x^2(s) = \sigma_{x\beta}^2(s) + \left[D_x(s)\sigma_p/p\right]^2. \quad (10)$$

Here, $\sigma_{x\beta}(s)$ represents the transverse width due to the betatron oscillation around the closed orbit while the term containing the dispersion function $D_x(s)$ accounts for the fact that ions with different momenta p oscillate around different equilibrium orbits. The average invariant action $E_x = \langle \epsilon_x \rangle$, representing the ion beam emittance, and $\sigma_{x\beta}(s)$ are related to each other by

$$\sigma_{x\beta}^2(s) = \tfrac{1}{2}\beta_x(s) E_x/\pi. \quad (11)$$

Thus, the r.m.s. beam size $\sigma_x(s_0) = \langle x^2 \rangle^{1/2}$ determined from a transverse beam profile at one position s_0 on the ring circumference yields the ion beam emittance in the corresponding direction after subtracting in quadrature the transverse width due to the ring dispersion and the momentum spread of the ion beam.

Since E_x is constant apart from slow variations due to beam heating and cooling, Eq. (11) can be used to derive the r.m.s. ion-beam size at any other position s on the ring circumference. Moreover, since the transverse ion angle $x' = \mathrm{d}x/\mathrm{d}s$ is represented by the derivative of Eq. (9), the emittance obtained from the beam-profile measurement at s_0 also yields the r.m.s. divergence $\sigma_{x'}(s) = \langle x'^2 \rangle^{1/2}$ at any position s. One finds that the divergence $\sigma_{x'}(s)$ is given in terms of $\sigma_{x\beta}(s_0)$ from Eq. (10) by

$$\sigma_{x'}^2(s) = \sigma_{x\beta}^2(s_0)\frac{1 + \alpha_x^2(s)}{\beta_x(s_0)\beta_x(s)} + \left[D_x'(s)\frac{\sigma_p}{p}\right]^2, \quad (12)$$

where $\alpha_x(s) = -(1/2)\mathrm{d}\beta_x/\mathrm{d}s$ and $D_x'(s) = \mathrm{d}D_x/\mathrm{d}s$. As the transverse ion velocity is $v_x = v_0 x'$, one also obtains the local transverse beam temperature for ions of mass M and average velocity v_0,

$$k_B T_x(s) = M v_0^2 \sigma_{x'}^2(s), \quad (13)$$

and the ion-beam temperature averaged over the ring circumference, defined by

$$\bar{T}_x = (1/C)\int_0^C T_x(s)\,\mathrm{d}s. \quad (14)$$

The relations given here basically apply to both the horizontal and the vertical direction, which in the following will be denoted by x and z, respectively. However, the corrections due to the ring dispersion in Eqs. (10) and (12) vanish for the vertical degree of freedom [$D_z(s) \equiv 0$] in a good approximation.

For a given resolution limit of the beam profile monitor, the precision of beam profile measurements also depends on the location of the monitor in the ring. A location with values of the lattice functions β_x, β_z as high as possible is preferable for measuring small emittances. The prototype BPM was installed at a position s_0 with $\beta_x(s_0) = 10$ m, a value close to the maximum for the normal operating mode of the TSR. At the position s_0' of BPM(XZ) we have $\beta_x(s_0') = 4.4$ m and $\beta_z(s_0') = 3.1$ m. The values averaged over the ring circumference are $\bar{\beta}_x = 6.4$ m and $\bar{\beta}_z = 3.7$ m for the normal operating mode. The dispersion function at both monitors is small [$D_x(s_0) \approx 0.3$ m, $D_x(s_0') \approx 0.5$ m] in normal operation; hence, for ion beams with a momentum spread of $\sigma_p/p < 10^{-4}$ the contribution of the ring dispersion to the horizontal beam size according to Eq. (10) is at most of the order of the spatial resolution.

4.2.2. Transverse electron cooling: cooling rate and cooling force

In the electron cooling device an electron beam of low longitudinal and transverse velocity spread, guided by a longitudinal magnetic field, is superposed on the ion beam in a straight section of the storage ring; the velocity of the electron beam is matched to the average ion-beam velocity. The length of the overlap region in the TSR is 1.5 m. By Coulomb scattering the ions transfer energy to the electrons, which are continuously replaced. In this way the transverse and the longitudinal temperature of the ion beam approach the temperature of the electron beam in its co-moving frame until an equilibrium between electron cooling

and heating of the beam (mainly by intrabeam scattering) is reached.

In first investigations with the prototype monitor we studied the cooling of a $^9Be^+$ beam with an energy of 0.81 MeV/u, corresponding to a beam velocity $v_0 = 1.26 \times 10^9$ cm/s. The energy of the cooler electrons was 425 eV at an electron current of 15 mA and an electron density of 3.7×10^6 cm^{-3}. Using laser fluorescence diagnostics [7] it was observed that the ions are cooled to a longitudinal velocity spread of $\Delta v_{\parallel} \lesssim 1 \times 10^5$ cm/s within ≈ 2 s. The transverse cooling was observed at the monitor by measuring horizontal beam profiles over intervals of 1 s at various delays after the injection (Fig. 12). All profiles were averaged over 10 injection cycles. For one of the measurements (see Fig. 12b), the ion beam size after the injection was limited by an aperture of 18 mm diameter installed on the ion orbit in the ring. This aperture has been removed for the second measurement (Fig. 12a), where the initial horizontal beam size is larger.

The horizontal component F_x of the cooling force as a function of the horizontal ion velocity v_x is shown schematically (neglecting in particular the vertical ion velocity v_z and the longitudinal ion velocity in the co-moving frame) in Fig. 13. For an ion velocity small compared to the effective electron velocity spread, the force approximately follows the linear dependence $F_x(v_x) = -kv_x$. If the magnetic guiding field of the electron beam is taken into account [3] (and is sufficiently strong as in the case discussed here with $B \approx$

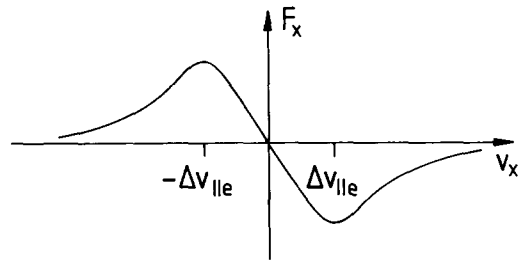

Fig. 13. Schematical plot of the transverse electron-cooling force F_x as a function of the transverse ion velocity v_x, showing the influence of the effective electron-velocity spread (given by the *longitudinal* velocity spread $\Delta v_{\parallel e}$ because of the magnetic guiding field of the electron beam).

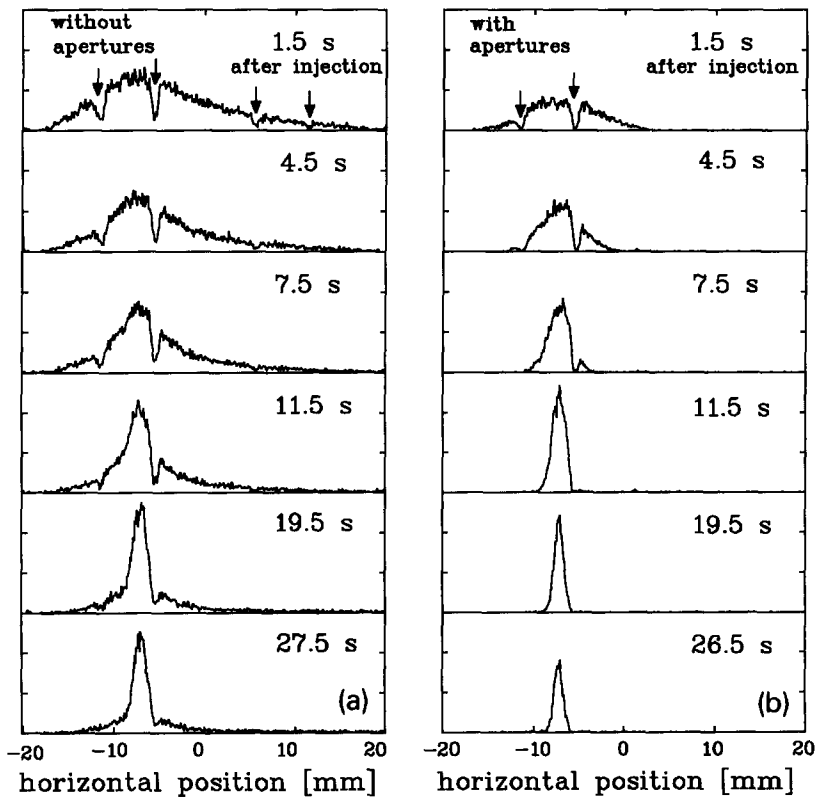

Fig. 12. Measurements of horizontal beam profiles of an electron-cooled $^9Be^+$ beam (0.81 MeV/u, initial current ≈ 1 μA) at different times after the injection for two situations: (a) no aperture was inserted; (b) the beam size was limited by an aperture of 18 mm diameter in the path of the stored ion beam. (The dips indicated by arrows are due to the calibration wires.)

14 mT), the position of the maximum of the cooling force is essentially given by the *longitudinal* electron velocity spread $\Delta v_{\|e}$, and the maximum force is increased considerably in comparison to estimates which do not account for the magnetic field. When the ion velocity becomes higher than the effective electron velocity spread, the cooling force decreases $\propto v^{-n}$ with $1 \le n \le 2$.

This velocity dependence of the electron cooling force causes fast cooling of ions of small betatron amplitudes and hence small transverse velocities ($v_x \lesssim \Delta v_{\|e}$) but a much slower cooling for ions with higher betatron amplitudes, as seen in Fig. 12. For small velocities $v_x \ll \Delta v_{\|e}$ the cooling decrement is approximately constant and close to its maximum reached at $v_x = 0$. On the other hand, the halo for the profiles taken without the aperture is formed by ions with $v_x \gg \Delta v_{\|e}$, which experience a smaller cooling force and hence much slower damping of the betatron motion. For the profiles taken with aperture, only ions which are already in the region $v_x \lesssim \Delta v_{\|e}$ can be stored and so no halo appears.

The measured beam size d_x (full width at half maximum) yields the horizontal ion velocity spread $\Delta v_x(s_c) = v_0 \sigma_{x'}(s_c)$ at the center position s_c of the electron cooler. The horizontal divergence is derived from Eq. (12) using the relation $\sigma_x = d_x/2\sqrt{2 \ln 2}$ and the value of $\beta_x(s_c) = 3.8$ m of the lattice function at the cooler. We obtain $\Delta v_x(s_c) = 1.0 \times 10^6$ cm/s for $d_x = 10$ mm (the typical beam size before cooling) and $\Delta v_x = 1.0 \times 10^5$ cm/s in the equilibrium ($d_x = 1$ mm). In comparison, the expected values of the transverse and the longitudinal r.m.s. velocity spread of the electron beam are given by $\Delta v_{x,e} = 1.3 \times 10^7$ cm/s and $\Delta v_{\|e} \approx 1 \times 10^6$ cm/s, respectively [30].

The beam size d_x extracted from the profiles neglecting the halo is shown in Fig. 14 as a function of the time after the injection. The slope of the function $d_x(t)$ represents the cooling decrement

$$\lambda_x = \frac{1}{\Delta v_x} \frac{\mathrm{d}(\Delta v_x)}{\mathrm{d}t} = \frac{1}{d_x} \frac{\mathrm{d}d_x}{\mathrm{d}t}. \tag{15}$$

Independent of the initial beam size, the highest transverse cooling rate $\lambda_{x,\max} = 0.38(2)\ \mathrm{s}^{-1}$ is reached at a critical beam diameter $d_{x,cr} = 8(1)$ mm (corresponding to about 5 mm at s_c) and then remains nearly constant while the transverse equilibrium is approached. The slow decrease for longer times (> 20 s) seen in the data taken without aperture is probably due to the reduction of the intrabeam-scattering heating rate as the stored ion current decreases.

In order to draw conclusions from the size of the cooling rate $\lambda_{x,\max}$ and the critical beam diameter $d_{x,cr}$, we consider the relation of the damping rate to the frictional force. In the range of the linear force law

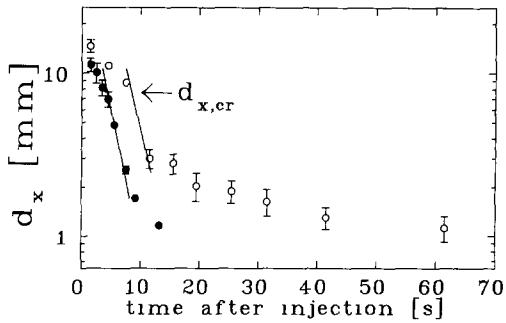

Fig. 14. FWHM beam size d_x as a function of the time after the injection extracted from the profiles in Fig. 12. For the closed symbols, the beam size was limited by the aperture of 18 mm diameter. For the open symbols no aperture was inserted. The straight lines indicate the steepest decrease of the beam diameter, corresponding to the maximum transverse cooling rate reached at a critical diameter $d_{x,cr}$.

$F_x = -kv_x$, the damping decrement becomes independent of the ion velocity spread and reaches its maximum given by

$$\lambda_{x,\max} = \eta_L k/2M, \tag{16}$$

where the factor 2 in the denominator stems from the averaging of the cooling force power $F_x v_x$ over the betatron phase. The fraction η_L of the storage-ring circumference occupied by the electron beam at the TSR is 0.022; this corresponds to the length of 1.2 m over which the angle between the electron and the ion beam is constant within ≈ 0.2 mrad, as concluded from magnetic-field measurements. From the measured maximum damping decrement of $\lambda_{x,\max} = 0.38(2)\ \mathrm{s}^{-1}$, we obtain a force constant of $k = 3.3(2) \times 10^{-6}$ eV s/m^2.

The position of the maximum of the cooling force $F_x(v_x)$ and hence the effective electron energy spread can be estimated from the critical beam diameter $d_{x,cr}(s_c)$ given above, which corresponds to $\Delta v_{x,cr}(s_c) = 0.8(1) \times 10^6$ cm/s. The maximum value $|F_x|$ of the cooling force reached close to $|v_x| = \Delta v_{x,cr}$ is given approximately by $k\Delta v_{x,cr} = 0.026(3)$ eV/m. In earlier measurements a *longitudinal* cooling force of close to 1 eV/m, given for a reference electron density of 10^8 cm^{-3}, was determined at a relative velocity of 1×10^6 cm/s [3]. Since the present measurement refers to a similar value of the relative velocity, but in transverse direction, it is plausible (and in fact supported by more detailed calculations of the electron cooling force in a magnetic field [31,32]) to expect a similar result for the size of the transverse cooling force. In fact, after multiplication with a factor of 10^8 cm$^{-3}/n_e$, the present experiment yields a maximum transverse cooling force of 0.71(9) eV/m, in a reasonable agreement with the longitudinal forces measured earlier.

The effective electron velocity spread $\Delta v_{x,\mathrm{cr}}$ agrees well with the expected longitudinal electron velocity spread of $\approx 1 \times 10^6$ cm/s. The corresponding longitudinal electron temperature is $k_B T_{\|e} = m(\Delta v_{x,\mathrm{cr}})^2 = 4(1)$ K, where m is the electron mass. Thus, the study of the beam profiles during electron cooling shows that also for the transverse cooling process the longitudinal electron temperature determines the shape and magnitude of the cooling force. In fact, this enhancement of the cooling force due to the magnetic guide field of the electron beam is decisive in providing fast cooling even for the heavy single-charged $^9Be^+$ ions and for an electron density which is relatively low because of the low beam velocity.

Meanwhile transverse electron cooling was studied with the method described above also for other ions ($^6Li^+$, $^7Li^+$, $^{12}C^{2+}$, $^{12}C^{6+}$, $^{18}O^{2+}$). A systematic analysis of the dependence of cooling times and cooling forces on ion and electron beam properties is in progress.

To get more detailed information about the velocity dependence of the transverse cooling force, also a study of the beam halo can be helpful. Such measurements are best interpreted using computer simulations of the electron cooling process. Haloes of the stored ion beam also occur in other situations and for other reasons and may considerably affect experiments performed in the ring. The profile monitors are of valuable help in detecting these effects.

4.2.3. Optimizing the alignment between electron beam and ion beam in the cooler section

To ensure optimal transverse cooling and a minimal ion beam diameter during experiments, the alignment between the electron beam and the equilibrium orbit of the stored ion beam has to be as good as possible. To this end, the direction of the longitudinal magnetic field guiding the electron beam can be varied by small angles θ_x and θ_z in horizontal and vertical direction with the help of correction coils. The optimum alignment is reached when the cooling time and correspondingly the cooling force assume their maximum value. In the present experiment with 0.81-MeV/u $^9Be^+$ ions, the FWHM horizontal beam diameter was measured 15 s after the injection for different settings of the correction coils. The result is shown in Fig. 15a and 15b, where the measured beam size is plotted as a function of the angles θ_x and θ_z, respectively. The zeroes of the angles correspond to the case when the correction coils are switched off. The horizontal beam diameter remains close to its minimum over the ranges $\theta_{0x} \pm \Delta\theta$ and $\theta_{0z} \pm \Delta\theta$. The increase is approximately symmetrical around the angles θ_{0x}, θ_{0z} for which the optimal alignment is achieved. Obviously, $\Delta\theta$ represents a critical misalignment angle at which the cooling rate λ_x decreases strongly. This decrease is expected

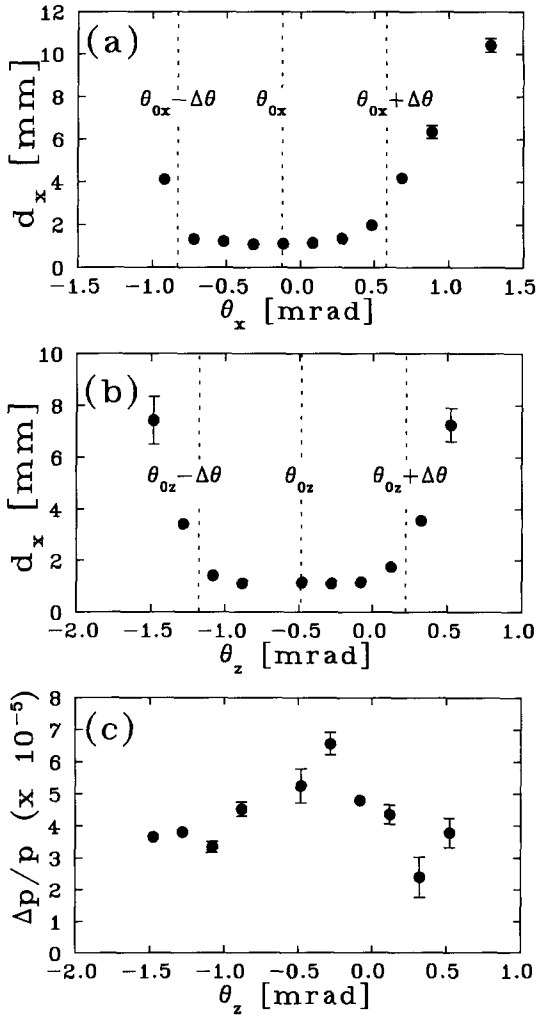

Fig. 15. Optimization of the alignment between electron and ion beam. Horizontal beam size (FWHM) d_x measured 15 s after the injection as a function of the electron-beam direction expressed by the angles (a) θ_x and (b) θ_z. (c) Relative momentum spread of the stored ion beam as a function of the vertical angle θ_z.

when the transverse velocity $v_0\Delta\theta$ associated with the misalignments exceeds the effective velocity spread of the electrons, $\Delta v_{\|e}$. The observed critical angle $\Delta\theta \approx 0.7$ mrad thus indicates an electron velocity spread of $\Delta v_{\|e} = v_0\Delta\theta \approx 0.9 \times 10^6$ cm/s and hence a longitudinal electron temperature of $T_{\|e} \approx 5$ K. This agrees well with the longitudinal temperature of 4(1) K determined independently (see section 4.2.2) from the critical beam size observed during the transverse cooling of an ion beam after injection. Other independent measurements of the longitudinal electron temperature at slightly different operating conditions of the electron

cooler also indicate similar values of the longitudinal temperature [30].

The longitudinal momentum spread $\Delta p/p$, obtained from the laser fluorescence diagnostics [7], is plotted as a function of the vertical angle θ_z in Fig. 15c. The highest longitudinal momentum spread occurs close to the optimal vertical angle θ_{0z}. This behaviour can be explained by the heating of the longitudinal ion motion by intrabeam scattering [33], which increases with growing ion density and hence with decreasing transverse size of the stored beam.

The described method of optimizing the alignment of the cooling electron beam to the equilibrium ion orbit has become a standard operational procedure at the TSR. The precision of < 0.1 mrad for the alignment achieved in this procedure apparently cannot be obtained by other techniques, such as observing the longitudinal momentum spread of the ion beam. Moreover, because of the high sensitivity this method can also be applied to low-intensity beams when other diagnostic tools as, e.g., the Schottky-noise measurements fail.

5. Summary and outlook

The residual-gas ionization beam profile monitors at the TSR have proven as important and very useful diagnostic devices for stored and cooled heavy-ion beams. The horizontal and vertical ion beam profiles can be measured in a non-destructive and sensitive way by single-ion detection of residual-gas ions liberated by the circulating ion beam. The minimal spatial resolution limit was found to be in the range of 0.2–0.3 mm (r.m.s.).

The monitors can be used for quantitative studies of the transverse beam behaviour during cooling and heating processes. The transverse cooling rates and the maximum transverse cooling force for the electron cooling of heavy-ion beams was determined from the time evaluation of the measured beam profiles. In addition, a sensitive method was found for optimizing the alignment between the cooling electron beam and the stored ion beam within ≈ 0.1 mrad. Further investigations concerning transverse electron cooling and the heating due to intrabeam scattering are in progress.

Acknowledgements

The authors wish to acknowledge the invaluable assistance of K. Bender, V. Mallinger, B. Vogt, T. Weber and the MPI workshops in the construction, manufacturing and installation of the beam profile monitors. The work has been supported by the German Minister for Research and Technology (BMFT) under contract number 06HD133I.

References

[1] E. Jaeschke et al., Proc. European Particle Accelerator Conf., vol. 1, Rome, 1988, ed. S. Tazzari (World Scientific, Singapore, 1989), p. 365.
[2] D. Habs et al., Nucl. Instr and Meth. B 43 (1989) 390; D. Habs, Nucl. Phys. News 1 (1991) 17, and refs. therein.
[3] H. Poth, Nature 345 (1990) 399; H. Poth, Phys. Rep. 196 (1990) 135.
[4] M. Steck, G. Bisoffi, M. Blum, A. Friedrich, C. Geyer, M. Grieser, B. Holzer, E. Jaeschke, M. Jung, D. Krämer, K. Matl, W. Ott and R. Repnow, Nucl. Instr. and Meth. A 287 (1990) 324; M. Steck, M. Blum, M. Grieser, E. Jaeschke, C.M. Kleffner, D. Krämer, W. Ott and R. Repnow, Proc. Workshop on Electron Cooling and New Cooling Techniques, Legnaro, 1990, eds. R. Calabrese and L. Tecchio (World Scientific, Singapore, 1991) p. 64.
[5] J. Javanainen, M. Kaivola, U. Nielson, O. Poulsen and E. Riis, J. Opt. Soc. Am. B 11 (1985) 1768.
[6] S. Schröder et al., Phys. Rev. Lett. 64 (1990) 2901.
[7] W. Petrich, M. Grieser, R. Grimm, A. Gruber, D. Habs, H.-J. Miesner, D. Schwalm, H. Wernøe, A. Wolf, R. Grieser, G. Huber, R. Klein, T. Kühl, R. Neumann and S. Schröder, Phys. Rev. A 48 (1993) 2127.
[8] J. Borer and R. Jung, Proc. CERN Accelerator School, Geneva, 1983, eds. P. Briant and S. Newman (CERN 84-15, Geneva, 1984) p. 385.
[9] D. Boussard, Proc. CERN Accelerator School, vol. 2, Oxford, 1985, ed. S. Turner (CERN 87-03, Geneva, 1987), p. 416
[10] W.H. DeLuca, IEEE Trans. Nucl. Sci. NS-16 (1969) 813.
[11] H. Weisberg, E. Gill, P. Ingrassia and E Rodger, IEEE Trans. Nucl. Sci. NS-30 (1983) 2179, and refs. therein.
[12] F. Hornstra, Hamburg report DESY HERA 87-25 (1987); and refs. therein.
[13] B. Vosicki and B. Zankel, IEEE Trans. Nucl. Sci. NS-22 (1975) 1475.
[14] G.I. Budker, N.S. Dikanskij, V.I. Kudelainen, I.N. Meshkov, V.V. Parkhomchuk, D.V. Pestrikov, A.N. Skrinskij and B.N. Sukhina, Part. Acc. 7 (1976) 197.
[15] M. Bell, J. Chaney, H. Herr, F. Krienen, and P. Møller-Petersen, Nucl. Instr. and Meth. 190 (1981) 237.
[16] M.B. Shah and H.B. Gilbody, J. Phys. B 15 (1982) 3441.
[17] D.S.F. Crothers and J.F. McCann, J. Phys. B 16 (1983) 3229.
[18] R.M. Sternheimer, Phys. Rev. 115 (1959) 137.
[19] R.K. Janev, L.P. Presnyakov and V.P. Shevelko, Physics of Highly Charged Ions (Springer, Berlin, 1985) p. 232.
[20] M.E. Rudd, Radiat. Res. 64 (1975) 153.
[21] High Voltage Power Supply Model NCE 20000-3, Heinzinger electronic GmbH, Rosenheim, Germany.
[22] Computer Code MAFIA, T. Weiland, Technische Hochschule Darmstadt, Darmstadt, Germany.
[23] Dual High Voltage Power Supply Model 8174, Novelec S.A., F-38244 Meylan, France.

[24] High Voltage Power Supply Model HNCEs 3000-1, Heinzinger electronic GmbH, Rosenheim, Germany.
[25] Model Chevron 3040 RAE for the prototype BPM and the vertical unit of BPM(XZ);
model Chevron 3115 RAE for the horizontal unit of BPM(XZ);
Galileo Electro-Optics Corp., Sturbridge, MA, USA.
[26] J. Wiza, Nucl. Instr. and Meth. 162 (1979) 587.
[27] E. Mathieson, Nucl. Instr. and Meth. 97 (1971) 171.
[28] G. Bisoffi, M. Grieser, E. Jaeschke, D. Krämer and A. Noda, Nucl. Instr. and Meth. A 287 (1990) 320.
[29] E.D. Courant and H.S. Snyder, Ann. Phys. (NY) 3 (1958) 1
[30] G. Kilgus, D. Habs, D. Schwalm, A. Wolf, N.R. Badnell and A. Müller, Phys. Rev. A 46 (1992) 5730.
[31] A.H Sørensen and E. Bonderup, Nucl. Instr. and Meth. 215 (1983) 27.
[32] A. Wolf, doctoral thesis, Univ. Karlsruhe, 1985 (Report KfK 4023, Karlsruhe, 1986).
[33] A.H. Sørensen, Frontiers in Particle Beams: Intensity Limitations, eds. M. Dienes, M. Month and S. Turner (Lecture Notes in Physics, vol. 400), (Springer, Berlin, 1992) p. 467.